Comprehensive Deformation Analysis of a Newly Designed Ni-Free Duplex Stainless Steel with Enhanced Plasticity by Optimizing Austenite Stability

MOHAMMAD MOALLEMI, ABBAS ZAREI-HANZAKI, MOSTAFA ESKANDARI, ANDREW BURROWS, and HOSSEIN ALIMADADI

A new metastable Ni-free duplex stainless steel has been designed with superior plasticity by optimizing austenite stability using thermodynamic calculations of stacking fault energy and with reference to literature findings. Several characterization methods comprising optical microscopy, magnetic phase measurements, X-ray diffraction (XRD) and electron backscattered diffraction were employed to study the plastic deformation behavior and to identify the operating plasticity mechanisms. The results obtained show that the newly designed duplex alloy exhibits some extraordinary mechanical properties, including an ultimate tensile strength of ~900 MPa and elongation to fracture of ~94 pct due to the synergistic effects of transformation-induced plasticity and twinning-induced plasticity. The deformation mechanism of austenite is complex and includes deformation banding, strain-induced martensite formation, and deformation-induced twinning, while the ferrite phase mainly deforms by dislocation slip. Texture analysis indicates that the Copper and Rotated Brass textures in austenite (FCC phase) and $\{001\}\langle110\rangle$ texture in ferrite and martensite (BCC phases) are the main active components during tensile deformation. The predominance of these components is logically related to the strain-induced martensite and/or twin formation.

I. INTRODUCTION

DUPLEX stainless steels (DSSs), which consist of a mixture of ferrite (BCC-α) and austenite (FCC-γ) phases, combine the advantages of ferritic and austenitic stainless steels. DSSs possess a higher strength and corrosion resistance compared with single-phase stainless steels, particularly when the fractions of ferrite and austenite are optimized. Conventional DSSs are heavy alloyed and classically have elemental compositions ranging from 18 to 26 Cr, 3 to 8 Ni, 1 to 5 Mn, and 1 to 2 Mo (all in wt pct).[1]

Similar to other structural materials, the development of advanced DSSs is conventionally accomplished by focusing on alloying so that improved mechanical behavior is achieved while considering the economic aspects. Accordingly, there have been many attempts to replace costly elements such as Ni and Mo with N and Mn, without degrading the corrosion and mechanical properties. The focus on a combination of Mn and N stems from the fact that (i) Mn increases the nitrogen (N) solubility and (ii) N and Mn have a synergistic effect on enhancing the mechanical properties and controlling the deformation mechanisms of the austenite constituent.[2–5]

The mechanical behavior of DSSs is influenced by the state of both austenite and ferrite phases. The ferrite deformation mechanism mainly involves dislocation slip owing to a high-stacking fault energy (SFE) and the presence of many slip systems.[6] It is worthy of note that in some alloy systems, deformation twins are also formed in ferrite during plastic strain.[7] Austenite deformation is more complex than that of ferrite and the active mechanisms are conventionally characterized by slip, mechanical twinning (resulting in twinning-induced plasticity, TWIP) and α'-(BCC) martensite formation (resulting in transformation-induced plasticity, TRIP).[8–10] These deformation mechanisms give rise to a strong work hardening effect and potentially to excellent plasticity, particularly where TRIP and/or TWIP is deliberately designed to take place over a wide

MOHAMMAD MOALLEMI and ABBAS ZAREI-HANZAKI are with the The Complex Laboratory of Hot Deformation & Thermomechanical Processing of High Performance Engineering Materials, School of Metallurgy and Materials Engineering, College of Engineering, University of Tehran, Tehran, 11365-4563, Iran. Contact e-mail: zareih@ut.ac.ir MOSTAFA ESKANDARI is with the Department of Materials Science & Engineering, Faculty of Engineering, Shahid Chamran University of Ahvaz, Ahvaz, 61357-43337, Iran. ANDREW BURROWS and HOSSEIN ALIMADADI are with the Technical University of Denmark, Center for Electron Nanoscopy, Fysikvej, Building 307, 2800 Kongens Lyngby, Denmark.
Manuscript submitted July 20, 2016.
Article published online May 30, 2017.

range of strain. Decreasing the SFE in the austenite phase stimulates twinning or strain-induced martensite (SIM) formation during deformation. When the SFE is low, perfect {111}⟨110⟩ lattice dislocations may dissociate into {111}⟨112⟩ Shockley partial dislocations and stacking faults would be formed in between them. Deformation bands, which arise from the accumulated formation and motion of such planar defects, can be formed as a result of the overlapping of stacking faults on {111} planes of the austenite during deformation.[11] Depending on the SFE, the deformation bands can be in the form of ε-(HCP) martensite, mechanical twins, or dense stacking fault bundles. A low-SFE energy favors the regular overlapping on every second {111} lattice plane and the formation of ε-martensite. The interaction of various such bands *i.e.* ε-martensite, promotes the formation of α′-martensite nucleation. In fact, the martensitic transformation and consequently TRIP effect in these materials typically follows the sequence of γ-austenite → ε-martensite → α′-martensite.[10–12]

A novel lean Mn-based DSS TRIP steel (Fe-19.9 Cr-0.42Ni-0.16 N-4.79Mn-0.11C-0.46Cu-0.35Si) has recently been developed by Herrera *et al.*[13] This alloy exhibits an ultimate tensile strength (UTS) of 1 GPa and an elongation to fracture above 60 pct after cold rolling and annealing treatment at 1423 K (1150 °C)/180 s. The martensitic transformation sequence ($\gamma \rightarrow \varepsilon \rightarrow \alpha'$) in TRIPing phenomena of this grade of steel could highly enhance the work hardening potential over a wide range of strain, thereby leading to enhanced ductility.

Choi *et al.*[14] studied the effect of varying the nitrogen content, from 0.1 to 0.35 wt pct, on TRIP behavior of their new series of DSSs. In their experiments, the enhancements of strength and ductility were attributed to the TRIP effect in the cold rolled and subsequently annealed material at 1373 K (1100 °C)/5 min. 1 GPa UTS and elongation to fracture of 60 pct for a steel containing 0.35 wt pct, N are reported. They have also developed a novel DSS in which an extended elongation to fracture (above 70 pct) was achieved by utilizing the TWIP mechanism.[15] Although the ductility of this DSS TWIP steel was higher than that of the TRIP DSS, its UTS was lower.

As previously mentioned, several studies have been performed on the strain hardening behavior due to either TRIP or TWIP effects. However, the design of a new alloy in which TRIP and TWIP simultaneously make a contribution to enhance the work hardening potential of an alloy has not been extensively investigated to date. Thus, the purpose of the present study was to concentrate on optimizing austenite stability so that TRIP and TWIP can synergistically enhance both UTS and elongation to fracture of the alloy during uniaxial tensile deformation. The strategy of designing the alloy in this work was to replace nickel by manganese and nitrogen in conventional nickel-chromium DSSs in order to design a new Ni-free DSS with low alloying cost and superior mechanical properties. Designing the alloy was performed using SFE analysis and the relevant findings of previous studies in the literature. In order to understand the deformation mechanism(s) of the present alloy, microstructural and textural characterizations were carried out after different levels of tensile deformation had been applied.

II. DESIGNING THE ALLOY

It is well understood that the design of a new alloy with a desirable high strength and high elongation to fracture, depends significantly on a precise understanding of the strengthening and deformation mechanism(s) of the alloy. In the case of DSSs, achieving enhanced mechanical properties is contingent on the deformation mechanisms of both austenite and ferrite phases. A comprehensive investigation of the microstructural evolution in DSSs during deformation at room temperature was performed by Fréchard *et al.*[16] According to their findings, the glide of dislocations inside the austenite grains and the grain orientation characteristics play an important role in plastic deformation of the austenitic constituent. For the ferrite phase, two mechanisms were considered. In the first one, the dislocations pile up in the austenite grains behind the phase boundaries that may give rise to local stress concentrations thereby generating dislocations in ferrite grains. The second mechanism is recognized to be the shearing of some ferrite grains because of the accumulated dislocations in the adjacent austenite grains.[16] While it is believed that the deformation mechanism in both austenite and ferrite phases is dislocation glide, the deformation characteristics may change according to chemical composition and deformation conditions. Recent studies by other researchers[2,3,15] reveal that the stability and plasticity mechanism of austenite can be affected by its chemical composition so that TRIP and/or TWIP mechanisms can be induced in the microstructure.

In the present study, a predetermined design strategy was conducted on a set of alloying elements to obtain optimum austenite stability. The design of the chemical composition was based on two concepts. On the one hand, the austenite should be sufficiently unstable such that a transformation-induced plasticity mechanism is initiated under loading. On the other hand, the austenite should be suitably stable so that TRIP and TWIP phenomena will occur over a wide range of strain, particularly at strains where TRIP and TWIP effects may prevent plastic instabilities.

The new alloy designed in this work uses Mn, C, and N instead of Ni as austenite stabilizing elements. In this alloy, Mn is not only a suitable alternative element as an austenitizing element but also may increase the solubility of interstitial elements such as C and N, which further enhances the austenite stability and leads to additional solid-solution strengthening. Nitrogen in this grade of steels serves to significantly improve the corrosion-resistance properties especially the resistance to localized corrosion. Nitrogen also retards the formation of detrimental intermetallic phases such as the sigma phase and delays sensitization.[17]

To obtain a duplex ferritic–austenitic structure, the chemical compositions of DSSs are generally composed of more than 18 wt pct Cr (arguably of higher interest,

between 20 and 22 pct). The amount of Cr in the designed alloy has been chosen to be around 20 wt pct to maintain a reasonable fraction of austenite in the microstructure. Regarding the other key elements, *i.e.*, Mn, N and C, it has already been shown that these elements strongly affect the austenite deformation mechanisms by influencing the SFE and dislocation configuration.[18–20] Lee *et al.*[20] evaluated the correlation between SFE and the deformation mechanism of the austenitic Fe-18Cr-10Mn steel containing a high concentration of interstitial elements (C, N). They calculated the SFE and found that there is a linear relationship between the measured SFE and the (N + C) content. They also showed that the deformation mechanism changes by increasing the interstitial elements in the following sequence: (i) deformation-induced martensitic transformation, (ii) a mixture of martensite transformation and twinning, (iii) twinning. It is true that Lee's studies generally consider the austenitic stainless steels, but Choi *et al.*[2] have applied Lee's investigations to clarify the TRIP effect in DSSs. According to previous findings,[2] the (C + N) content should be around 0.3 wt pct to activate TRIP effects in the alloy. The findings of Herrera *et al.*,[13] Ran *et al.*,[21] and Choi *et al.*[2] on the deformation behavior of DSSs show that TRIP effects can be successfully activated in DSSs when the alloy contains from 4 to 6 wt pct Mn. The resulting SFE of the austenite constituent is low enough to effectively let the transformation of austenite to martensite to occur. Therefore, a higher Mn content should be used to activate both the TRIP and TWIP phenomena during deformation. It should be noted that, besides the TRIP and TWIP mechanisms, solid-solution hardening effects, particularly solute strengthening by N and Mn, play a synergistic role in the overall strengthening of the alloy. Regarding the higher levels of N and Mn contents in the designed steel in this study, solid-solution strengthening is more pronounced compared with conventional DSSs. In addition, the absence of Ni in the chemical composition of the present alloy has reduced the adverse effects of decreasing N solubility. Indeed, the substitution of Ni with Mn would increase the solubility of nitrogen resulting in a larger interstitial solid-solution hardening effect compared with conventional alloys.

The currently available models, calculate SFE of austenite in a fully austenitic structure but unfortunately, there is no model to calculate the SFE for medium Mn steels with a duplex structure. The designed alloy in the present study is not fully austenitic. Therefore, it was expected that the SFE calculations would not lead to precise values but would provide a reasonable estimate for the SFE level alloys. The thermodynamic model applied by Curtze *et al.*[22] was used to calculate the SFE when designing the alloy. Based on this model, the austenite SFE value is extracted from the following equation:

$$\gamma_{fcc} = 2\rho\Delta G^{\gamma \rightarrow \varepsilon} + 2\sigma^{\gamma/\varepsilon} \qquad [1]$$

where ρ refers to the density of atoms in the close-packed plane of {111} (close to the theoretical density of {111} plane), $\Delta G^{\gamma \rightarrow \varepsilon}$ the molar free energy of

the $\gamma \rightarrow \varepsilon$ phase transformation, and γ/ε the interfacial energy between γ and ε phases. By means of reasonably accurate values for $\Delta G^{\gamma \rightarrow \varepsilon}$ and $\sigma^{\gamma/\varepsilon}$, the austenite SFE can be estimated. Based on the SFE calculations, the ideal concentration of Mn was determined to be about 8 wt pct in the newly designed alloy. The calculated SFE was ~22 mJ/m^2 for the austenite constituent, an amount higher than the corresponding SFE values of other DSSs in the literature, which showed only a TRIP but not TWIP effect.[2] The chemical composition of the designed DSS was 20Cr-8Mn-0.3N-0.02C. The phase diagram of this steel was constructed using Thermo-Calc software (Figure 1). The austenite and ferrite fractions after annealing at 1373 K (1100 °C) were calculated to be 74 and 26 pct, respectively.

III. EXPERIMENTAL PROCEDURE

A. *Materials and Methods*

The chemical composition of the designed DSS is given in Table I. The alloy was prepared using an induction furnace under nitrogen atmosphere, followed by the pressure electroslag remelting process. The remelted ingots with dimensions of 50 mm × 70 mm × 700 mm were homogenized at 1373 K (1100 °C) for 120 minutes, hot rolled at temperatures between 1373 K and 1473 K (1100 °C and 1200 °C) to a final thickness of 20 mm, and finally solution annealed at 1373 K (1100 °C) for 30 minutes. The solutionized material was cut perpendicular to the hot-rolling direction and machined to workpieces in the form of plates of 5 mm thickness. The workpieces were cold rolled from 5 to 1 mm thickness (~80 pct area reduction) and annealed at 1373 K (1100 °C) for 180 seconds; the workpieces were finally quenched in water. To examine the mechanical properties, flat tensile specimens were machined parallel to the rolling axis according to the ASTM E8 standard. Interrupted tensile tests to different strain levels at ambient temperature were carried out using a universal tensile machine.
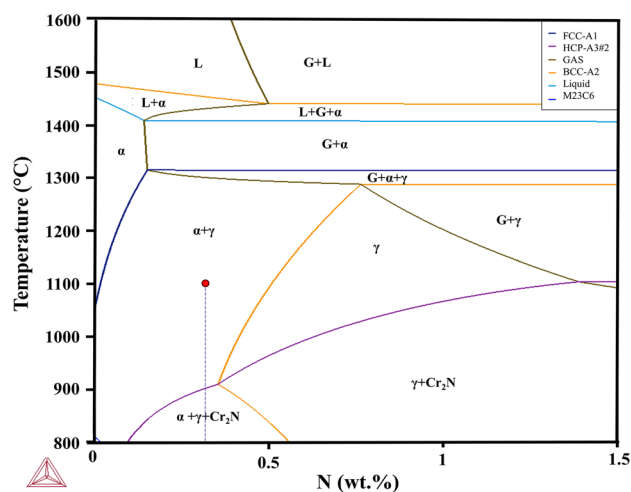

Fig. 1—The equilibrium phase diagram of the newly designed DSS obtained by Thermo-Calc.

Grade	C	Cr	Mn	N	Ni	Si
DSS	0.02	20.02	8.21	0.32	0.05	0.36
TRIP DSS*	0.11	19.9	4.79	0.16	0.42	0.35

*The DSS designed by Herrera et al.[13].

B. Phase Characterization

Crystallographic phase characterization was performed using a Ferritescope (Fischer MP30) and X-ray diffraction (XRD Philip's X'Pert Cu-Kα mode). The XRD scan speed was 3 deg/min, and the voltage and current were 40 kV and 200 mA, respectively. The texture measurement was carried out using a Bruker D8 advanced diffractometer with Cr Kα radiation and a 2D Hi-star detector. Before XRD, the specimens were electro-polished to remove any possible deformation-induced martensite on the surface. The electrolyte used was 200 mL $HClO_4$ + 800 mL ethanol at 30 V. To observe both the austenite and ferrite grain boundaries by optical microscopy, specimens were electro-etched in a 65 pct nitric acid solution at 1 V.

To characterize the microstructure before the tensile test, electron backscattered diffraction (EBSD) was performed on an electro-polished sample. EBSD measurements were performed in an FEI Helios Nano-Lab™ 600 equipped with an EDAX-TSL EBSD system and a Hikari camera. The EBSD measurement was carried out following a hexagonal grid with an electron probe current of 5.5 nA at an acceleration voltage of 18 kV, with a step size of 500 nm.

The OIM 6™ software suite was used for the analysis of the acquired EBSD data. Post-acquisition treatment of the recorded EBSD data included the following cleaning steps using routines available in the OIM 6™ software. First, the confidence index (CI) of every point in the map within a recognized grain was assigned to the highest confidence index CI value found in that grain (a grain was defined as a region consisting of at least three connected points with a misorientation of less than 5 deg). Secondly, by so-called grain dilation, a point with an orientation which does not belong to any grain is considered to correspond to the same orientation of the majority of neighboring points. Afterward, all data points with CI less than 0.1 were disregarded. To characterize the twin boundaries in FCC, the $\sum 3$ boundaries were studied using the CSL model based on Brandon's criteria (i.e. allowing for a deviation of 8.6 deg).[23]

For EBSD analysis, after tensile testing, a part of the specimen was cut and mechanically ground using SiC papers, followed by polishing with 3 and 1 μm diamond pastes at the final stage. The samples were then vibratory polished using 0.04 μm colloidal silica slurry for 12 hours. EBSD data were acquired using a Hitachi SU6600 field emission scanning electron microscope (FE-SEM), equipped with a Nordlys Nano Oxford detector. The EBSD measurements were carried out following a square grid with an acceleration voltage of 20 kV, and a step size of 180 nm. The HKL CHANNEL5 software suite was used for the analysis of the acquired EBSD data.

IV. RESULTS AND DISCUSSION

A. Stepwise Deformation Characterization

1. Mechanical properties and flow behavior

The deformation characteristics of the newly designed DSS were analyzed at different stages of plastic deformation. The flow behavior of the newly designed DSS was compared with a TRIP DSS (the chemical composition is given in Table I as the reference alloy) to explain the plasticity mechanisms. The engineering and true stress–strain curves, and the strain hardening rates (SHR) (dσ/dε) of the newly designed and reference alloy[13] are presented in Figure 2(a) through (c), respectively. As seen in Figure 2(a), the designed duplex alloy exhibits superior mechanical properties (combination of UTS~900 MPa and very high elongation to fracture of 94 pct). A comparison of the mechanical properties between the designed DSS and some advanced high strength steels is shown in Table II. It can be seen that the designed alloy has a high yield stress (YS) and UTS (~900 MPa), and a significantly enhanced total elongation to fracture (~94 pct). This means the modulus of toughness (the area under stress–strain curve up to fracture) is noticeably high in the newly designed DSS. Since the actual stress–strain curves reported in the literature are not available to the present authors, UTS × EL is used as a rough estimate of the toughness, and tabulated in Table II. For the newly designed DSS, the resultant UTS × EL is about 8.3 GPa which is higher than that of all other advanced high-strength steels. This means that the designed alloy can be a suitable candidate for automotive materials where crash-type deformations and a high amount of absorbed energy are needed.

Figure 2(b) shows the true stress–strain curves of experimental DSS and reference TRIP alloy. Both steels exhibit a sigmoidal shape in their respective true stress–strain curves (Figure 2(b)); however, it is more pronounced in the reference alloy. Stage-wise behavior is typically observed in TRIP assisted steels. Regarding the strain hardening behavior, the SHR of the newly designed steel (Figure 2(c)) is generally lower than that of the reference alloy. The SHR curves of both alloys display similar behavior in the sense that both curves show a minimum followed by a subsequent maximum; these extrema represent the occurrences of TRIP and/or TWIP phenomena during straining. The SHR curve of
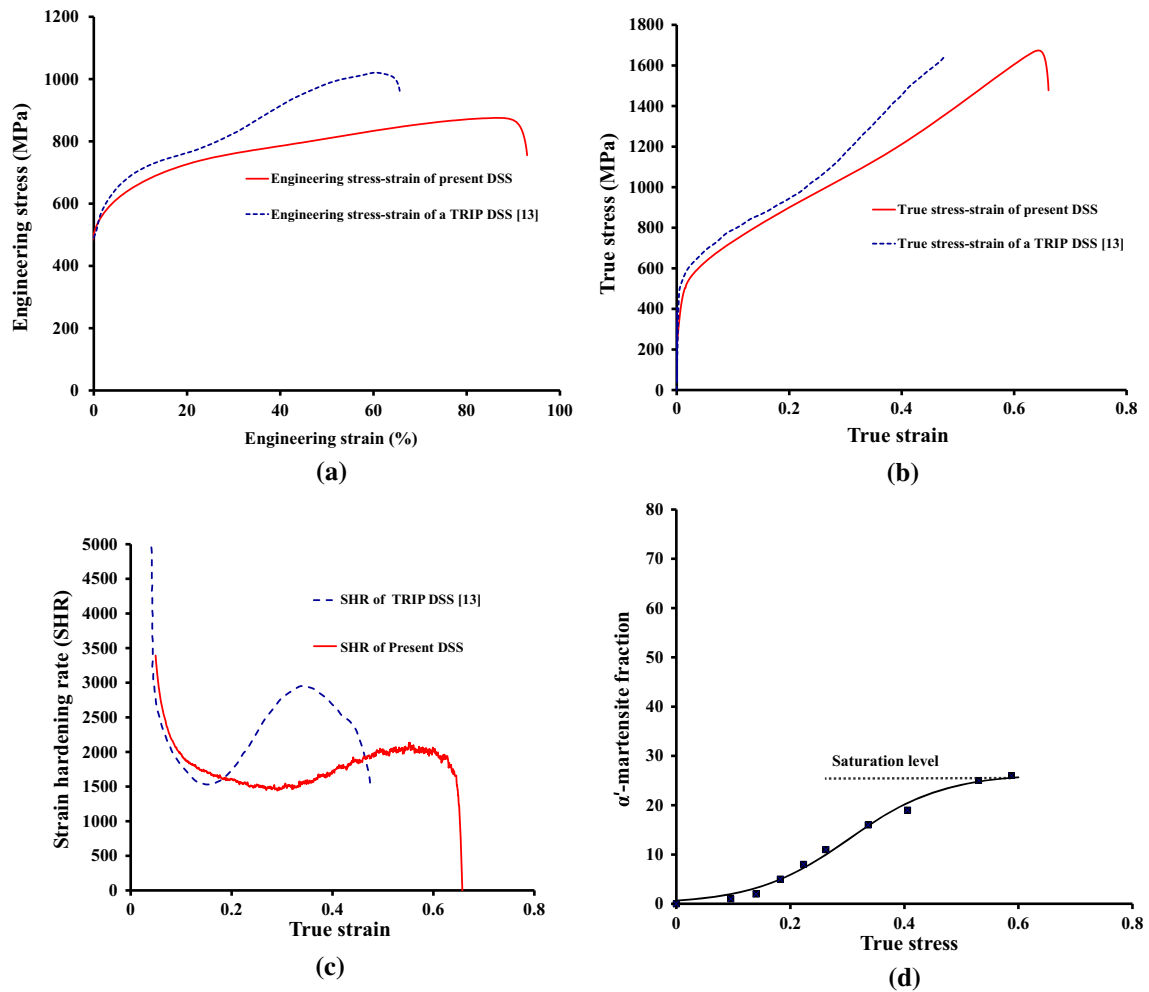
Fig. 2—(a, b) Engineering and true stress–strain carves, and (c) the variations of strain hardening rates (SHR) of the newly designed steel in comparison with the reference TRIP DSS one[13]; (d) the volume fraction of α'-martensite as a function of true strain in the newly designed steel.

Table II. Mechanical Properties of the Newly Designed Duplex Material Compared with Some Advanced High-Strength Steels

Chemical Composition (Wt Pct)	Initial Microstructure Before Deformation	Yield Strength (YS) (MPa)	Ultimate Tensile Strength (YS) (MPa)	Elongation (EL) (Pct)	EL × UTS (GPa Pct)	References
25Mn-3Si-3Al	γ	260	640	95	6.1	24
20Mn-3Si-3Al	$\gamma + \varepsilon$	300	840	80	6.7	24
15Mn-3Si-3Al	$\gamma + \varepsilon + \alpha$	440	920	45	4.1	24
16.5Cr-8Mn-3Ni-2Si-1Cu-0.25N-0.08Ti	γ	350	700	70	4.9	25
19.9Cr-0.42Ni-0.16N-4.79Mn-0.11C-0.46Cu-0.35Si	$\gamma + \alpha$	500	1020	65	6.6	13
20Cr-3Mn-2Cu-2Si-2Ni-0.2N	$\gamma + \alpha$	550	820	70	5.7	15
20Cr-8.2Mn-0.32N	$\gamma + \alpha$	530	890	94	8.3	present work

the newly designed alloy starts to increase at $\varepsilon = 0.27$ and after reaching a maximum at $\varepsilon \approx 0.55$, it gradually reduces until approaching the fracture strain. The increase of SHR is related to SIM formation during plastic deformation. The first inflection point of the reference alloy[13] occurs at a lower strain level, which is attributed to the lower stability of the austenite. Hence, SIM transformation is triggered more easily in the

reference TRIP alloy, and the inflection point appears at the lower strain level. The metastability of both alloys will be discussed in thermodynamic terms in the next section.

In order to make a logical relation between the SHR and SIM formations, the volume fractions of α'-martensite in the newly designed steel at different levels of strain are presented in Figure 2(d). As seen from the figure, the
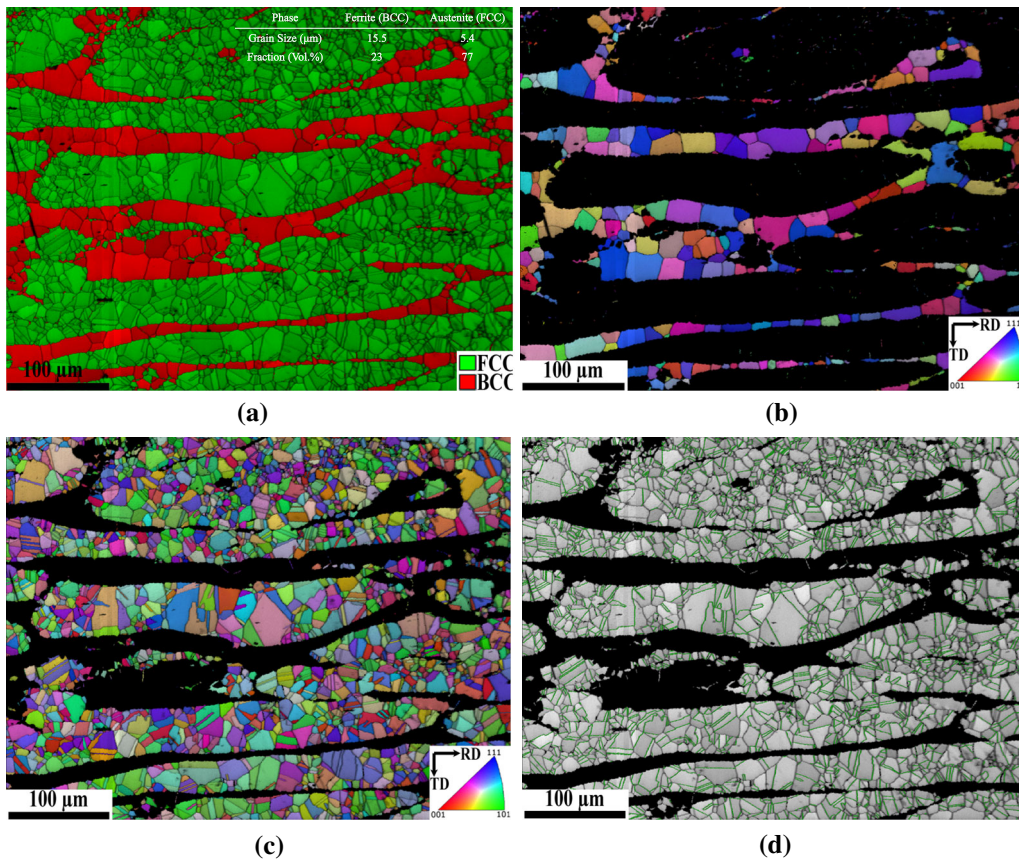
Fig. 3—The EBSD maps of the newly designed DSS after full annealing treatment: (*a*) IQ map superimposed with phase distribution map; IPF map superimposed with IQ map of (*b*) ferrite and (*c*) austenite; (*d*) twin boundary map of the austenite constituent.

volume fraction of α'-martensite increases up to $\varepsilon \approx 0.55$ and then becomes saturated. This strain level, *i.e.*, $\varepsilon \approx 0.55$, is close to the strain at which the SHR curve starts to decrease. This indicates that, after TRIP saturation, the strain is mostly accommodated by the remaining austenite and the ferrite; these phases induce lower strain hardening than TRIP phenomena in the microstructure, and thus the rate of hardening decreases.

2. Microstructural evolution

The EBSD analysis of the newly designed DSS before tensile deformation is presented in Figure 3. The image quality map superimposed with the phase map in Figure 3(a), shows the microstructure consists of a bamboo-like structure of coarse ferrite grains elongated in the rolling direction and coarse equiaxed austenite grains. The austenite and ferrite grain sizes were found to be 5.4 and 15.5 μm, respectively. The orientation map of austenite and ferrite in Figures 3(b) and (c). shows clearly the difference between ferrite and austenite grain size. A twin boundary map of the austenite phase in Figure 3(d), also reveals that there are many twin boundaries in austenite, manifested in the low SFE nature of this constituent.

The corresponding microstructures at different strain levels are illustrated in the optical micrographs shown in Figure 4. In the initial stage of deformation

(e = 10 pct) at room temperature, a heterogeneous distribution of deformation bands is revealed inside the austenite grains (arrowed in Figure 4(a)); these bands might be mechanical twins and/or ε-martensite bands. With further deformation up to e = 20 pct (Figure 4(b)), the density of the deformation bands increases, and they intersect with each other inside the austenite grains so that the α'-martensite can be partially formed at intersected areas. The SIM phase at intersected areas has been indicated with white arrows. A few of these deformation bands are identified as ε-martensite using XRD phase analysis (Figure 5). The pattern obtained from the specimen deformed up to e = 20 pct indicates the presence of the $(101)\varepsilon$ reflection of ε-martensite . However, due to the relatively high background signal of other ε-martensite reflections, the other reflections are not that obvious. Upon increasing the plastic strain to e = 30 pct (ε = 0.26), the densities of deformation bands, which are partly indexed as ε-martensite (Figure 5), and consequently the areas at which they intersect, increase in the microstructure (Figure 4(c)). At this level of deformation, the α'-martensite may well nucleate at the deformation band intersections and in the vicinity of interphase and/or grain boundaries. This causes the α'-martensite fraction to gradually increase with tensile strain. It can be confirmed by the X-ray patterns (Figure 5), which exhibit an increase in the relative intensity of BCC (α'/α)
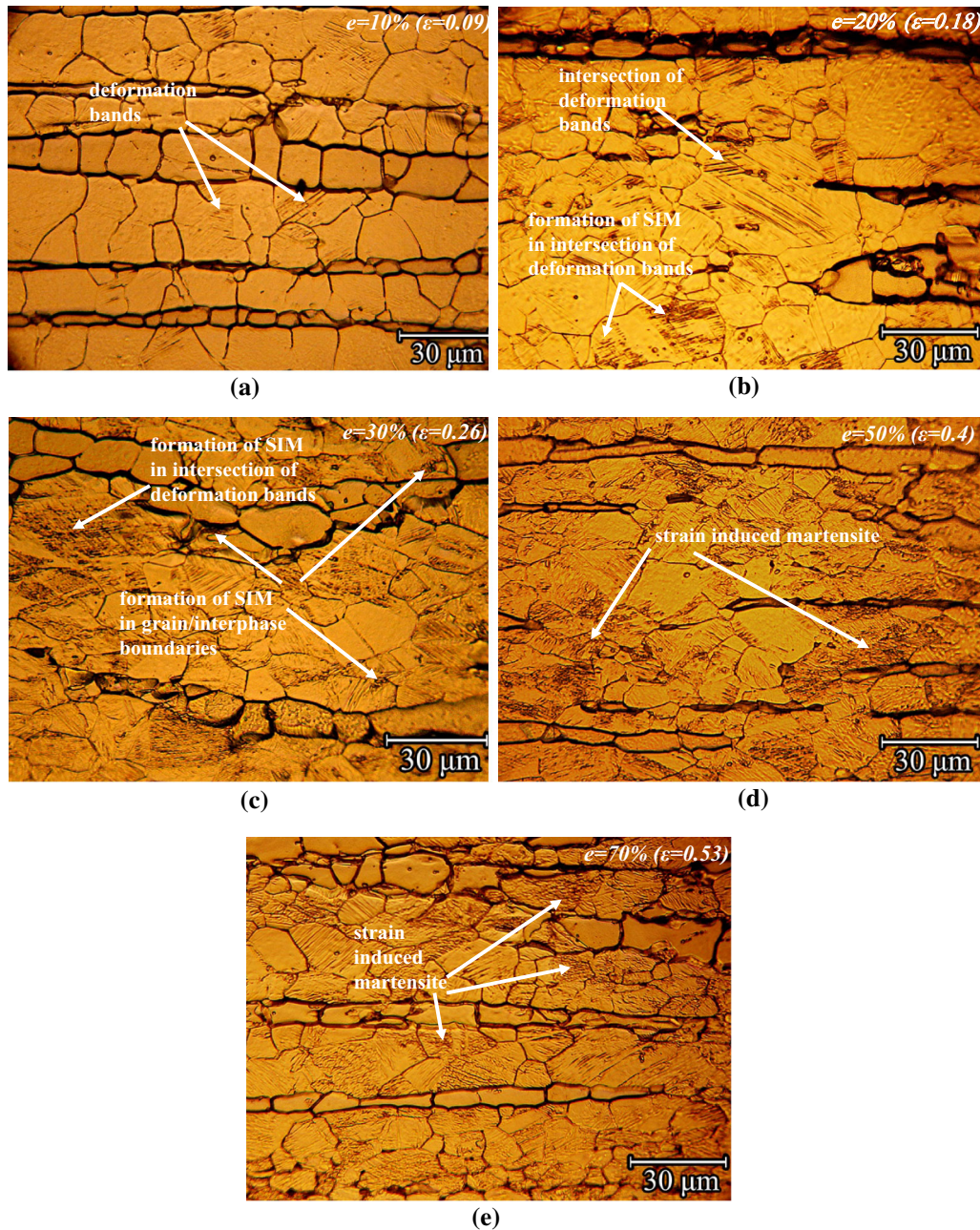
Fig. 4—Optical micrographs of the newly designed alloy cold tensile elongated to (*a*) *e* = 10 pct, (*b*) *e* = 20 pct, (*c*) *e* = 30 pct, (*d*) *e* = 50 pct, and (*e*) *e* = 70 pct.

to austenite (γ) with strain, due to the strain-induced α'-martensite formation. These explanations suggest that the austenite transforms to α'-martensite through nucleation at ε-martensite intersections and at interphase/grain boundary areas. The former, *i.e.*, the sequential $\gamma \rightarrow \varepsilon \rightarrow \alpha'$ transformation, was originally discussed by Olson and Cohen.[26,27] Their model explains that superimposed shearing, created by intersecting two ε-martensite bands, may lead to a total distortion that shifts the original austenite lattice close to the final α'-martensite structure.

In general, the formation of strain-induced α'-martensite gives rise to an upsurge in the SHR curve associated with a TRIP effect. This effect is directly related to the volume of already formed α'-martensite. In the present case, the SHR curve (Figure 2(c)) does not show an increase as soon as α'-martensite starts to form, but when the volume of α'-martensite reaches a high level which overcomes the decreasing contributors of SHR. In other words, the increase in the SHR value due to martensite formation is compensated by lower strain hardening of the ferrite phase at the initial stages of deformation. Following Figure 2(d), α'-martensite is detected upon straining to a relatively low level (ε = 0.15), but the increase in SHR does not occur until ε = 0.3 strain, at which point the volume fraction

of α'-martensite is about 20%. The microstructural observations shown in Figure 4 and the corresponding XRD patterns (Figure 5) for specimens strained greater than $e = 30$ pct (*i.e.*, $e = 50$ pct and $e = 70$ pct) clearly demonstrate the progress of α'-martensite formation in the austenite microstructure. However, once the α'-martensite reaches a saturation level, around
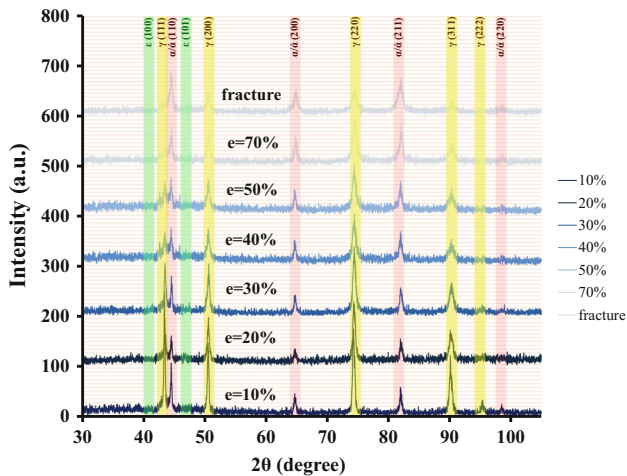

Fig. 5—The X-ray patterns of specimens deformed to different levels of tensile engineering strain.

$\varepsilon = 0.55$ (Figure 2(d)), the SHR curve starts to drop due to the reduction of the α'-martensite role in strain hardening behavior as discussed above.

Figure 6 shows the EBSD results of a specimen strained to $e = 30$ pct ($\varepsilon = 0.26$). The corresponding phase map of the deformed alloy is given in Figure 6(a). Since EBSD cannot differentiate effectively between BCC ferrite and body-centered tetragonal (but near BCC) martensite, the phase map does not reflect the presence of martensite. In order to locate the martensite in the maps, it is necessary to include image quality (IQ) values for phase separation purposes. For the case of martensite, this phase contains a higher number of lattice defects which leads to a lower IQ. Hence, to differentiate between two BCC and near BCC phases (*i.e.* α'-martensite and ferrite), the phase map has been superimposed on the IQ map. The α'-martensite areas, which are formed inside austenite grains, are indicated by white arrows. For better clarification, inverse pole figure (IFP) images of FCC and BCC phases are given in Figure 6(b, c), respectively. As seen in the figure, the α'-martensite has nucleated in the vicinity of grain boundaries and heavily deformed areas inside the grains. Unfortunately, the high dislocation density subsequently created has led to diffuse patterns, and thus indexing was difficult. As a result, the deformation bands that are observed in optical micrographs cannot be clearly identified in the EBSD maps.
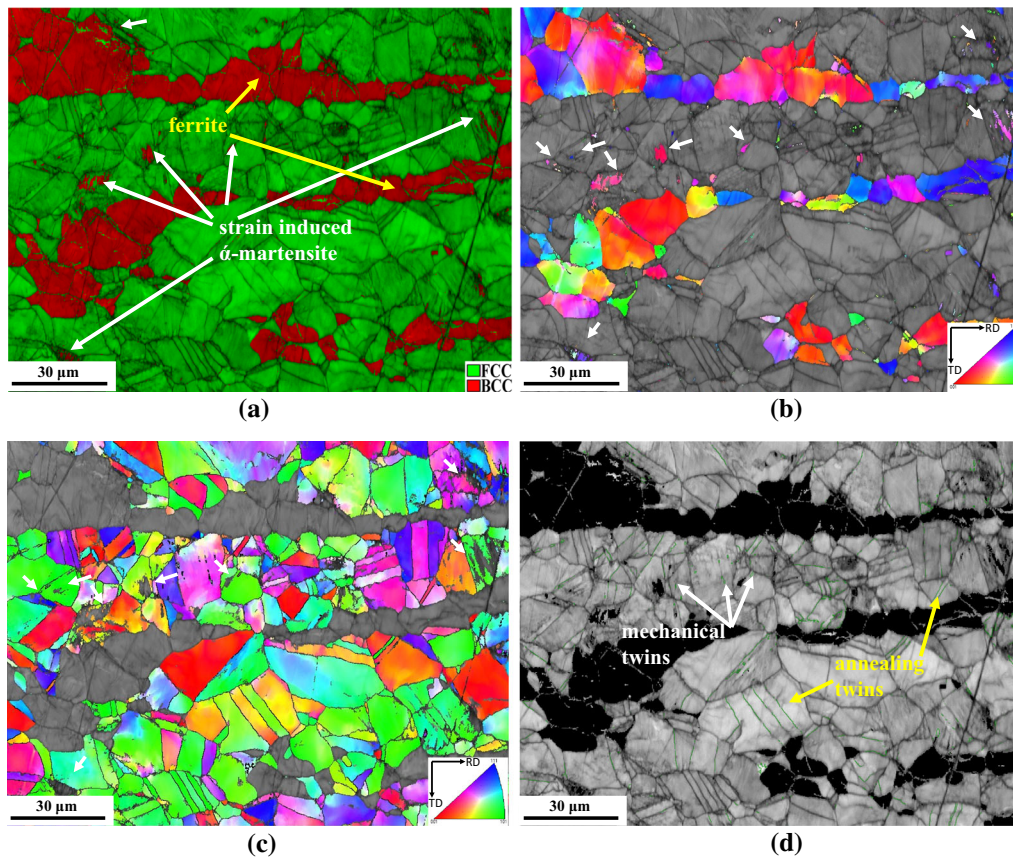

Fig. 6—(a) the EBSD phase mapping image of experimental DSS after $e = 30$ pct engineering tensile strain. The corresponding IPF images of (b) BCC phase (c) FCC phase; the area related to the strain-induced α'-martensite indicated by white arrows, and (d) FCC twin boundary map.
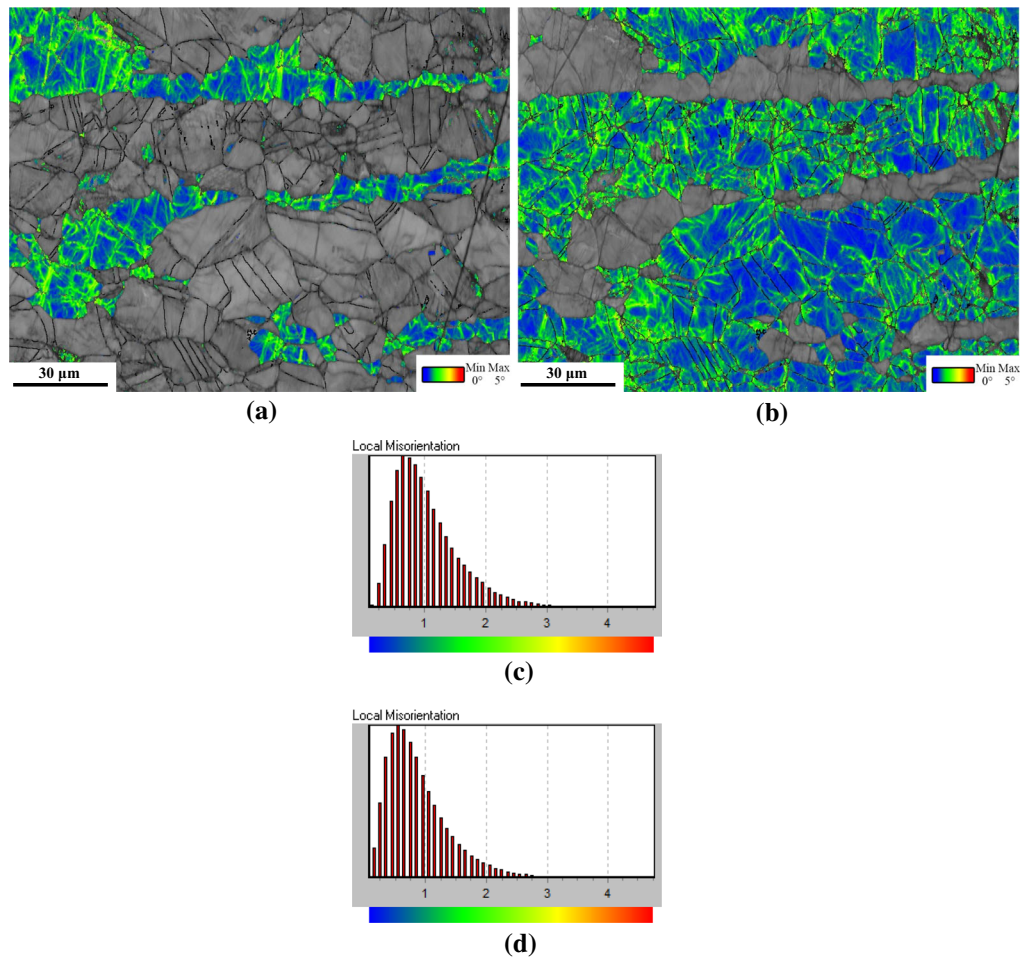
Fig. 7—KAM maps of the newly designed DSS after e = 30 pct engineering tensile strain for (*a*) BCC phase, and (*b*) FCC phase, the corresponding KAM distribution for (*c*) BCC phase, and (*d*) FCC phase.

Figure 6(d) shows the twin boundary map of austenite. As seen in the figure, besides the presence of annealing twins (parallel bands arrowed in austenite grains), some mechanical twins (non-parallel and/or lenticular-like bands arrowed in austenite grains) can be characterized in the deformed microstructure. Formation of mechanical twins and their effects on the mechanical properties have been addressed in the literature for FCC metals, especially copper[28,29] and steel.[30,31] Twin boundaries are effective barriers to dislocation motion, thus enhancing the mechanical strength, on the one hand. On the other hand, twin boundaries can accommodate dislocation storage.[28,32,33] Thus, twins can simultaneously enhance the strength and ductility.[29,34] This suggests that deformation-induced twinning and strain-induced α'-martensite can synergistically control the strain hardening of the DSS. The formation of mechanical twins during low and moderate strain levels, *i.e.*, where α'-martensite content is not sufficiently high, brings about work hardening, and suppresses a sudden decreasing of work hardening rate. Thus, TWIP and TRIP phenomena have a synergistic effect on the work hardening behavior of the alloy.

It has been well known that the SFE of austenite determines its plastic deformation mechanism.[35] The SFE of the austenite phase in the newly designed DSS, based on its chemical composition, is calculated to be 22 mJ/m^2, which is within the activation range of TRIP/ TWIP mechanisms.[36] However, the SFE value of austenite can change with deformation. Mahato *et al.*[37] investigated the deformation behavior of a Fe-Mn austenitic steel. They believe that the effective SFE of austenite increases with strain. This is related to the strain energy of stacking faults (SFs) per unit area, which is influenced by the dislocation character and density. Increasing the SFE value of the austenite phase during deformation may promote mechanical twin formation in this constituent.[37] However, in addition to SFE, short range ordering (SRO) phenomena also play an important role in controlling the deformation mechanisms in favor of twin formation.[18,38] As is reported, increasing the nitrogen content in high-nitrogen steels would promote the formation of mechanical twins through SRO effects. Under such a condition, the SRO stimulates slip planarity in the microstructure through a glide plane-softening phenomenon.[39] Behjati *et al.*[18] reported that the formation of mechanical twins
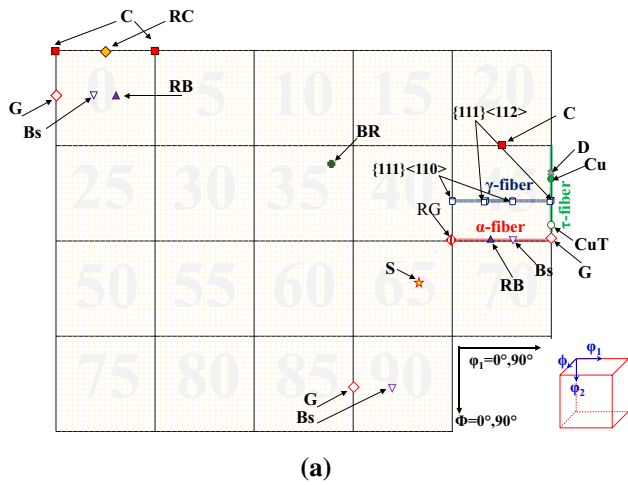
(a)
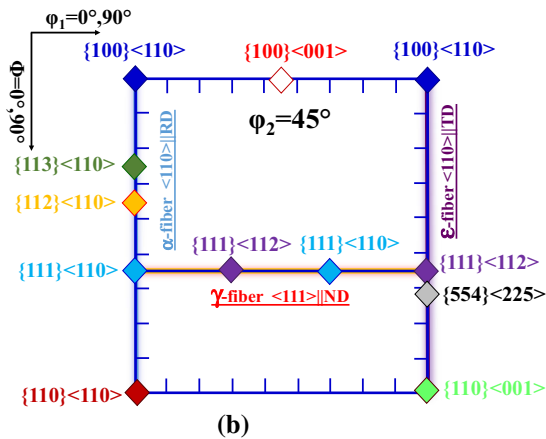
(b)

Fig. 8—Typical orientation distribution function (ODF) of (*a*) austenite (*b*) ferrite (section φ_2 = 45 deg). The main components: C-Cube, G-Goss, RG- Rotated Goss, BS- Brass, BR- Brass Recrystallization, D-Dillamore, RB- Rotated Brass, Cu-Copper, CuT-Copper Twin, and S-S orientation.

in a steel with 0.39 wt pct nitrogen could be associated with dislocation planar glide. Based on Thermo-Calc computation results, the austenite phase in the newly designed DSS under the aforementioned annealing condition consists of 0.43 wt pct nitrogen. The solute nitrogen may lead to a planar dislocation arrangement, and this in turn assists in the short-range atomic ordering between N and transition metals such as Mn and Cr (*i.e.*, those located at the left of Fe in the Periodic Table). Therefore, under such conditions, the formation of mechanical twins would be expected.

To better understand the deformation behavior of each constituent, the Kernel Average Misorientations (KAM) of each phase, namely the BCC phase (ferrite and α′-martensite) and the FCC austenite phase for the specimen deformed up to *e* = 30 pct are illustrated in Figures 7(a) and (b), respectively. The KAM maps serve as a measure of the deformation-induced local orientation gradients inside the grains. The KAM map of the ferrite phase shows in-grain orientation gradients, which are related to areas with a high density of dislocations. It also shows that the highest local misorientation is located at

the ferrite/ferrite and ferrite/austenite interfaces, where high dislocation densities exist. This suggests that the ferrite is deformed by a dislocation glide mechanism so that the dislocation density can be at a high level at grain and/or interphase boundaries. The area related to α′-martensite shows high KAM values due to the presence of an increased number of defects. The KAM map of austenite shows a high level of misorientation close to the deformation band, twin boundaries, and α′/γ and α/γ interfaces. Figures 7(c) and (d) show the KAM distribution of BCC and FCC phases, respectively. As seen in the figure, the corresponding KAM related to the peak value is a little higher for BCC (~0.7) than that for FCC (~0.5) at this level of strain (*e* = 30 pct). This is related, on the one hand, to the α′-martensite formation with an increased number of defects and, on the other hand, to the softer nature of the ferrite phase which accommodates more strain than austenite in the initial stages of deformation.

All in all, the superior mechanical properties (specifically total elongation of about 94 pct), of the newly designed DSS compared with the reference steel (Figure 2) are ascribed firstly, to the TWIP effect which has not been observed in the reference TIRP DSS and secondly, to the optimized austenite stability, which is higher than that of austenite phase in the reference alloy. The austenite stability can be described in terms of the chemical driving force of γ-austenite-to-α′-martensite transformation ($\Delta G^{\gamma \to \alpha'}(T)$). According to Kaufman,[40] $\Delta G^{\gamma \to \alpha'}(T)$ of the ternary solid solution of Fe-Cr-Ni system can be determined as follows:

$$
\begin{aligned}
\Delta G^{\gamma \to \alpha'}(T)(J\,\text{mole}^{-1}) = {} & (1 - X_{\text{Cr}} - X_{\text{Ni}})(5048.4 - 1.01 \\
& \times 10^{-2}T^2 + 6.46 \times 10^{-6}T^3) \\
& + X_{\text{Ni}}(-15540 + 2.97 \times 10^{-3}T^2 \\
& + 1.64 \times 10^{-7}T^3) \\
& + X_{\text{Cr}}(1932 + 4.2 \times T) \\
& + X_{\text{Ni}}(1 - X_{\text{Cr}} - X_{\text{Ni}}) \\
& (15120 + 2.43T(1 - \ln T)) \\
& - 26040X_{\text{Ni}}X_{\text{Cr}} \\
& + X_{\text{Cr}}(1 - X_{\text{Cr}} - X_{\text{Ni}}) \\
& \times (-11760 + 3.15T)
\end{aligned}
$$

[2]

where X_{Cr} and X_{Ni} are the mole fractions of Cr and Ni, respectively. In order to take into account the influences of other alloying elements such as C, N, Mn, Mo, and Si that have strong effects on the driving force, the Ni_{eq} (Ni equivalent) and Cr_{eq} (Cr equivalent) were used to calculate $\Delta G^{\gamma \to \alpha'}$ based on the following equations[41]:

$$\text{Ni}_{\text{eq}} = \text{Ni} + 0.31\text{Mn} + 22\text{C} + 14.4\text{N} + \text{Cu} \quad [3]$$

$$\text{Cr}_{\text{eq}} = \text{Cr} + 1.4\text{Mo} + 1.5\text{Si} + 3\text{Ti} + 2\text{Nb} \quad [4]$$

The corresponding $(-\Delta G^{\gamma \to \alpha'})$ values for the newly designed DSS and the reference alloy were calculated to be ~1356 and ~1507 J/mol, respectively. The lower value
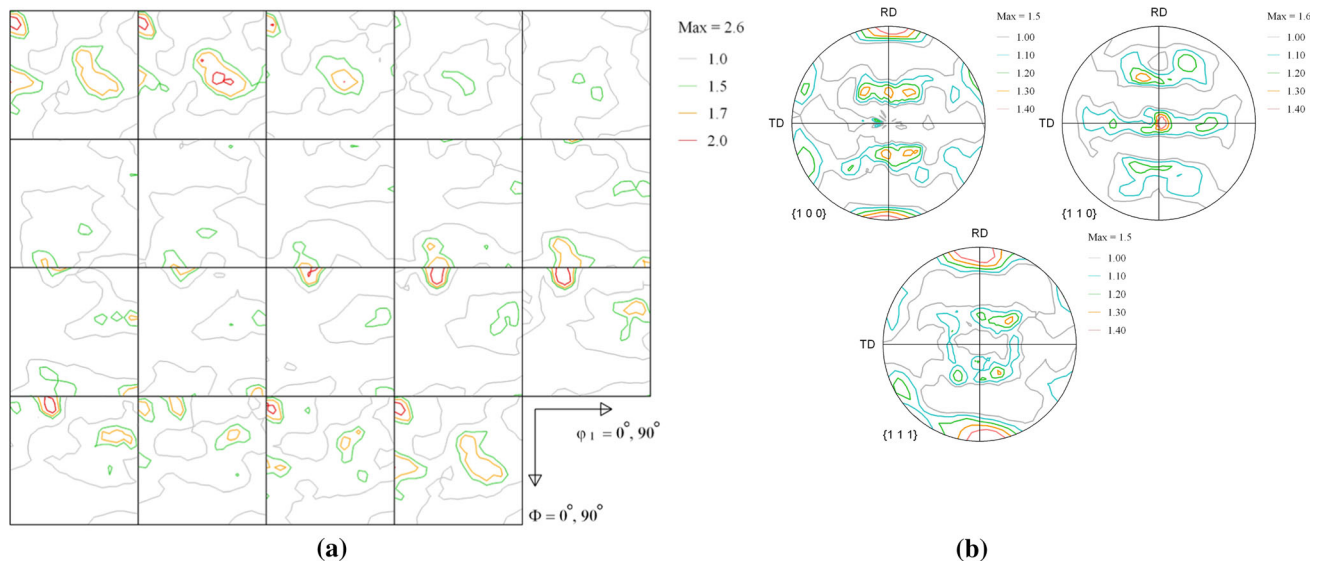
Fig. 9—The (a) ODF (b) pole figure presentation of FCC-austenite texture in newly designed DSS for pre-deformed specimen.

Table III. The Volume Fraction of the Predominant Orientations in Pre-deformation and After Tensile Deformation of Austenite Phase of the Newly Designed DSS

Component	Component Fraction (Pct)		
	Pre-deformation	30 Pct Engineering Tensile Strain	70 Pct Engineering Tensile Strain
Cube {001}⟨100⟩	2.64	3.59	3.95
Goss {011}⟨100⟩	3.08	4.4	4.4
Cu {112}⟨111⟩	5.9	8.9	11.4
Brass {011}⟨211⟩	4.94	6.28	6.48
S{123} ⟨634⟩	10.93	12.76	13.51
Rotated Cube {001}⟨011⟩	1.25	0.81	0.64
Rotated Goss {011}⟨011⟩	2.49	1.09	0.78
Rotated Cu {112}⟨110⟩	3.49	1.47	1.18
Rotated Brass {011}⟨111⟩	6.76	10.25	13.20
Brass Recrystallization {236}⟨385⟩	8.73	6.52	5.86
F {111}⟨112⟩	3.27	3.8	3.4
E {111}⟨110⟩	3.37	1.14	1.12
Copper Twin {552}⟨115⟩	3.70	4.90	4.66
Dillamore {4 4 11}⟨11 11 8⟩	5.49	7.5	9.2

of $(-\Delta G^{\gamma \rightarrow \alpha'})$ in the newly designed material reveals that the austenite phase needs a higher mechanical driving force for the $\gamma \rightarrow \alpha'$ transformation to occur dynamically during plastic straining. Indeed, the TRIP effect in this alloy can be activated at a higher strain level where strain hardening reserves are usually more desirable to reach a higher uniform deformation. Under such conditions, the TRIP effect can effectively postpone plastic instability and enhance plasticity of the alloy. Accordingly, the higher total elongation of the newly designed steel compared with reference is justified.

B. Texture Aspects

1. Pre-deformation texture

The most important texture components and fibers in the austenite and ferrite are presented in the form of orientation distribution functions (ODF) in Figure 8. The

ODF maps of macro-texture analysis by means of XRD and related pole figures of the austenite constituent are shown in Figures 9(a) and (b). For better clarification, the volume fractions of the main texture components are given in Table III. The austenite texture consists mainly of Goss {011}⟨100⟩, S {123}⟨634⟩, Copper {112}⟨111⟩, Rotated Brass {011}⟨211⟩, Brass Recrystallization {236}⟨385⟩ and relatively weaker Cube {001}⟨100⟩ orientation. As is well established, the first three orientations are the main components in the cold-deformed FCC materials.[42,43] Texture development in FCC materials is related to their SFE levels.[42–48] Here, the formation of a strong Brass Recrystallization component {236}⟨385⟩ can be related to the low SFE of the austenite constituent, i.e., Brass Recrystallization texture is a main component upon annealing low-SFE FCC materials.[47,48]

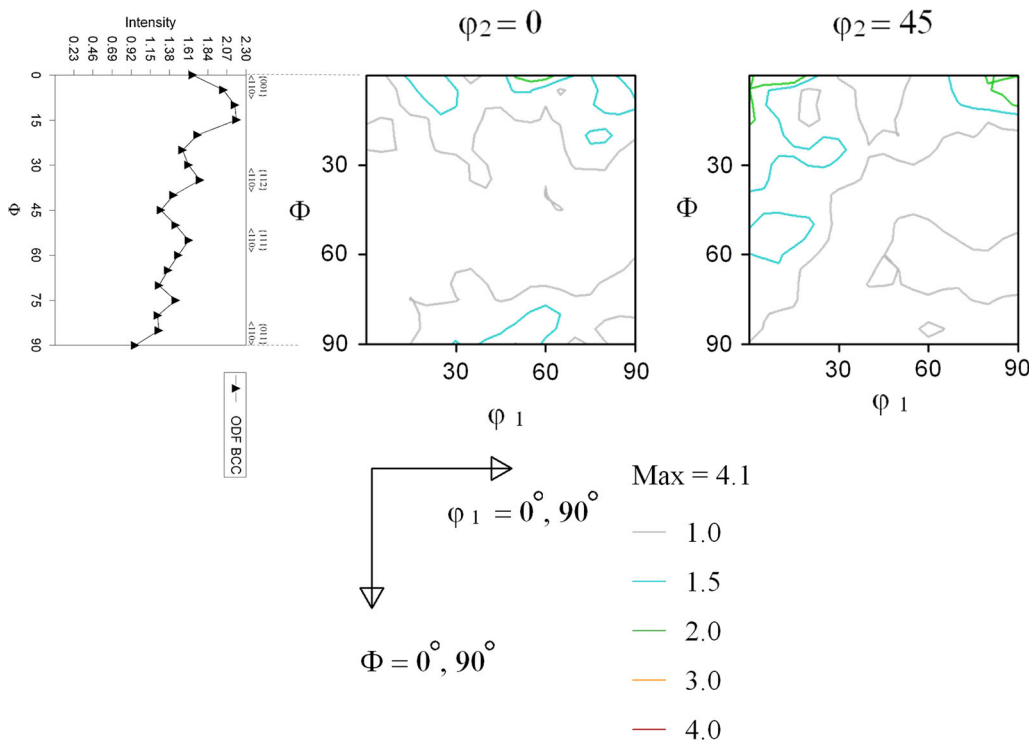The other austenite texture components are deformation orientations specifically S, Copper, Goss, and

Fig. 10—The $\varphi = 0$ deg, 45 deg ODF sections of BCC-ferrite constituent in the newly designed DSS before tensile deformation.

Dillamore (which is a first order twin of the Goss orientation). The retention of deformation texture in austenite after annealing can be due to factors such as short annealing time (only 180 seconds) and suppressed growth selection. Regarding the latter, this can occur as a result of the low mobility of grain boundaries due to solute drag effects. The high nitrogen content of this alloy most likely reduces the grain boundary mobility during recrystallization of the austenite phase of DSS and leads to texture retention after annealing. In addition, the reversion of α'-martensite (which has been formed during previous cold rolling) to austenite and the subsequent recrystallization would influence the texture of reversed austenite. As well reported previously, if the reversion transformation ($\alpha' \rightarrow \gamma$) occurs successfully, the austenite phase develops a sharp texture consisting of Brass $\{110\}\langle112\rangle$, Copper $\{112\}\langle111\rangle$ and S $\{123\}\langle634\rangle$, beside Goss $\{110\}\langle001\rangle$ orientations.[49] Accordingly, the presence of these components is expected in the austenite phase of the newly designed material, based on the whole history of treatment. The other main component in austenite orientation, i.e. Rotated Brass $\{110\}\langle111\rangle$ was also observed under annealing conditions of single phase austenitic low-SFE alloys.[50,51] The formation of the Dillamore orientation (which is a twin order of the Goss$\{110\}\langle001\rangle$ orientation) is also justified by the low-SFE level of austenite in favor of twinning formation during recrystallization.

The pre-deformation BCC ferrite texture is shown by the ODF sections ($\varphi_2 = 0$ deg, 45 deg) in Figure 10. Considering the texture map of the ferrite phase (Figure 8(b)), the ferrite annealing texture in the newly designed duplex alloy mainly consists of $\{001\}\langle110\rangle$,

$\{112\}\langle110\rangle$ and $\{111\}\langle110\rangle$ orientations as well as the $\{111\}\langle112\rangle$ orientation (albeit with a significantly lower intensity). As shown in Figure 10, the ferrite phase exhibits the α-fiber texture, the intensity of which decreases toward the $\{111\}\langle110\rangle$ orientation. Although α-fiber is a predominant fiber in cold-deformed ferritic steels,[42] the ferrite phase in the present DSS shows α-fiber texture after annealing. This can be attributed to the short annealing time i.e. the texture is inherited in the present condition. Keichel et al.[52] found that recovery and subsequent recrystallization were responsible for the remaining $\{001\}\langle110\rangle$ and $\{112\}\langle110\rangle$ components in the ferrite phase of cold-deformed DSSs. They also reported that the annealing texture of the ferrite phase in DSSs strongly resembled the annealing texture of single phase ferritic steels and did not indicate any influence by the concurrent second phase i.e. austenite.[52] Therefore in the present study, remnants of the $\{001\}\langle110\rangle$, $\{112\}\langle110\rangle$ orientations can be justified in this way. However, in the present case, the constraint of interphase boundaries between ferrite and austenite can impede the rotation of ferrite grains during annealing and help the texture inheritance of ferrite phase.

2. Tensile deformation texture

The texture analysis of the FCC austenite phase corresponding to the specimens deformed up to $e = 30$ pct and $e = 70$ pct tensile strain is illustrated in Figure 11. Figures 11(a) through (d) represent the ODF maps and related pole figures, respectively. In addition, the fraction of components is given in Table III. As seen in the figure, the fractions of Copper,
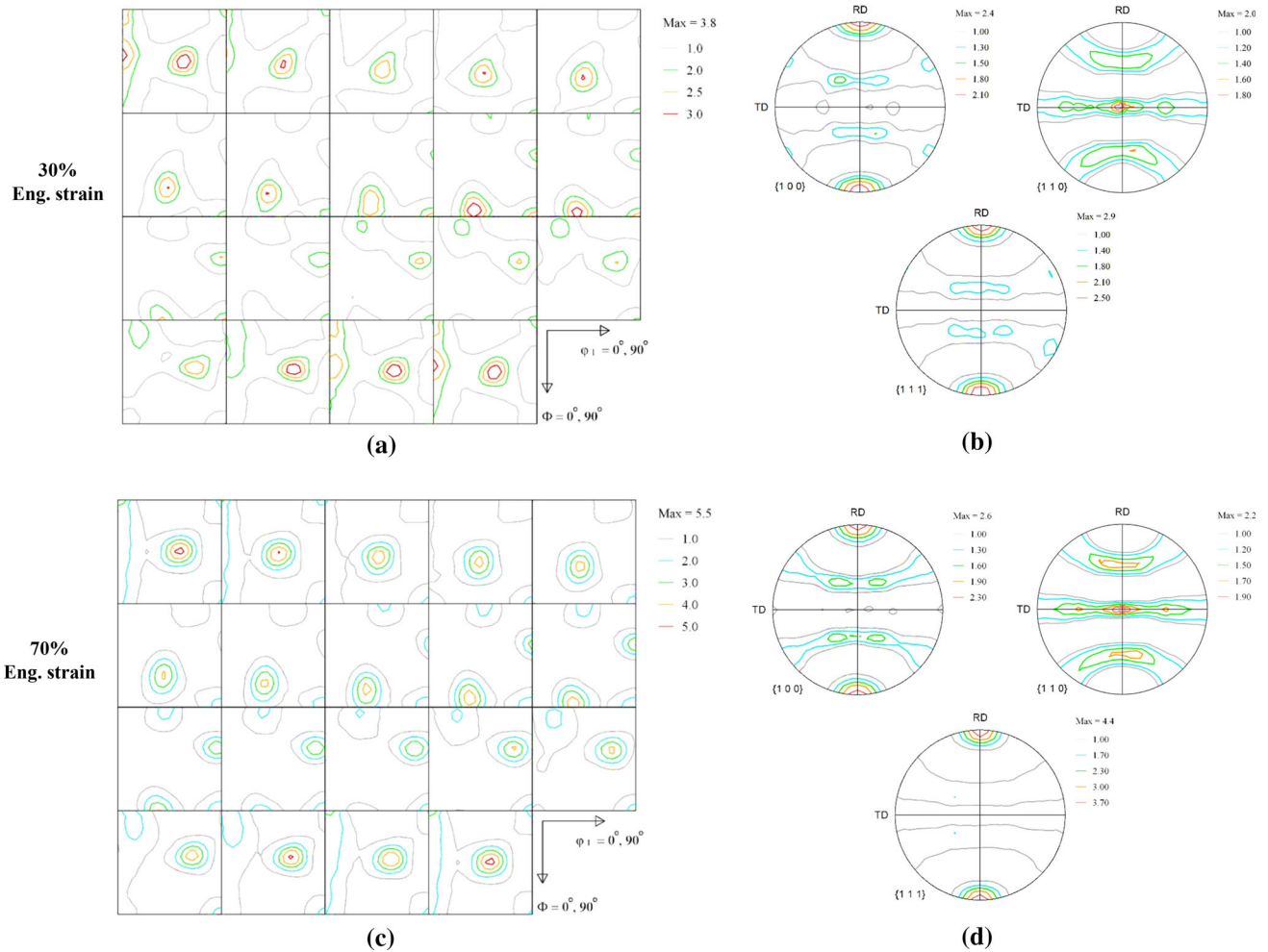
(a)

(b)

(c)

(d)

Fig. 11—The ODF and poles figure texture presentation of FCC phase for specimens deformed up to (*a*, *b*) 30 pct (*c*, *d*) tensile 70 pct engineering strain.

S, Dillamorem and Rotated Brass orientations are significantly increased, while the Brass and Goss orientations remain almost constant; however, the fraction of Brass Recrystallization orientation is significantly decreased.

The SFE is known to strongly affect the development of the crystallographic texture during cold deformation (in the present case room temperature tensile deformation). High SFE materials at room temperature, which deform by dislocation slip, develop a Copper or pure metal texture. Low SFE materials, develop a texture with a lower intensity on the Copper component and with higher intensity on the Goss, and Brass components.[45,53–55] Due to the low SFE of the austenite phase in the newly designed steel, the latter components are expected to be formed in the austenite phase. However, the intensities of Dillamore and Rotated Brass components are increased by deformation, while those of Goss and Brass components, despite a low SFE, do not undergo a significant change under strain (Table III).

Although the general tendency of austenite texture development in low-SFE austenite phase is the formation of a Brass texture, the texture development in a metastable austenite phase is also affected by the strain-induced α'-martensite transformation.[56] The formation of strain-induced α'-martensite is expected to weaken the development of the Brass texture.[56] This has been explained by the fact that grains with a $\langle 100 \rangle$ axis parallel to the direction of principal stress were found resistant to martensitic transformation. Clearly, the Goss orientation $\{011\}\langle 100 \rangle$ conforms to this criterion while the Brass orientation $\{011\}\langle 211 \rangle$ does not.[57,58] In addition, the deformation mode, *i.e.*, tensile and/or compression mode, can affect the texture component development during straining. Most of the literature is focused on the cold-rolled (compression mode) state, and the direct comparison of texture components between tensile-deformed material and compression-deformed one is not correct. Militisky *et al.*[59] reported that the Rotated Brass component (instead of pure Brass component) developed during tensile deformation of a set of metastable Ni-free austenitic stainless steels. Therefore, in the present case, insignificant change in Brass component with deformation can be related, on the one hand, to the SIM transformation resulting from the sluggish texture
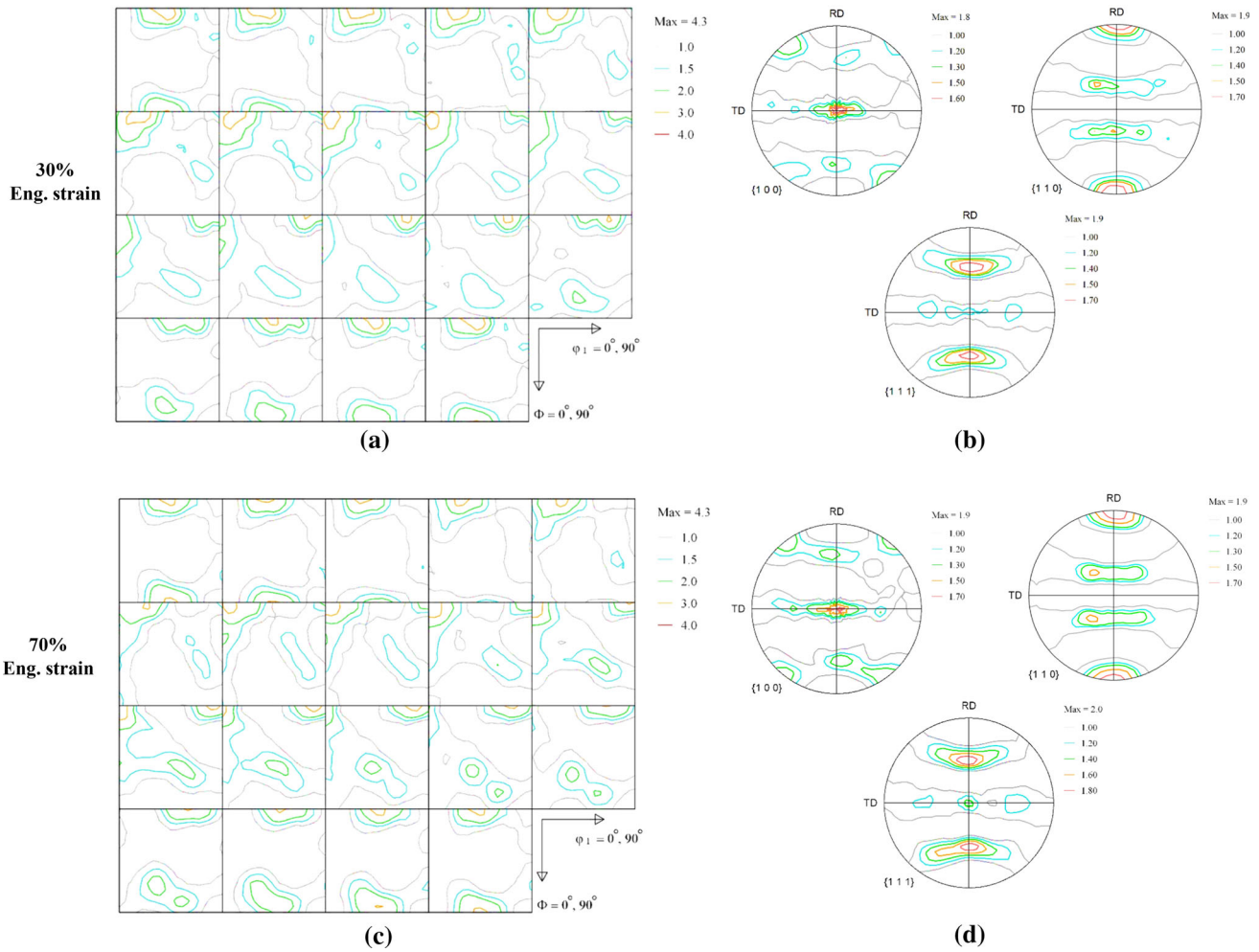
Fig. 12—The ODF and poles figure texture presentation of BCC phase for specimens deformed up to (*a*, *b*) 30 pct (*c*, *d*) tensile 70 pct engineering strain.
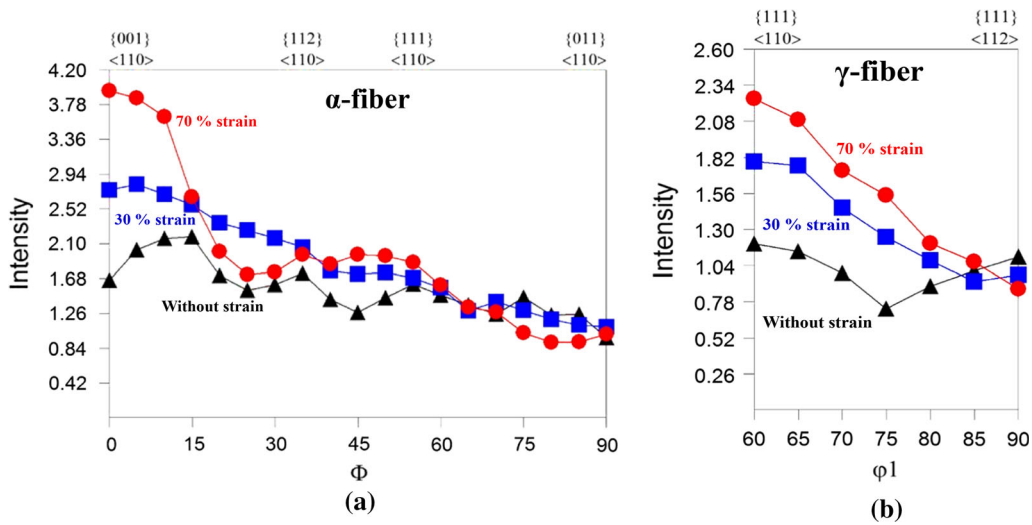

Fig. 13—The evolution of (*a*) α-fiber and (*b*) γ-fiber of BCC phase in the newly designed DSS during tensile deformation.

development and, on the other hand, to the tensile-deformation mode. The presence of a weak Goss component in the present work can be interpreted by the increase in the Dillamore orientation population (which is the first order of the Goss-twinned orientation) instead of pure Goss orientation.

The development of the Copper orientation in the low-SFE austenite phase is not generally expected. The initial explanation for the formation of this orientation in such low-SFE material would be deformation localization. It is believed that flow localization in deformation bands would result in localized adiabatic heating. This increases the SFE of the austenite constituent thereby forcing the texture toward the Copper texture direction.[51] On the other hand, the fact that the austenite phase has developed a sharp Copper texture instead of pure Brass may be interpreted by the presence of deformation bands, specifically twins, in the microstructure as follows. Plastic deformation is initially started by dislocation glide. The twins are initially formed on the {111} plane having the highest resolved shear stress. This primary twin system would extend across the grain. Although the twin fractions are not enough to make a "twinning volume effect" and thus contribute directly to texture development, the twins indirectly affect the deformation texture. Multiple slips by the activation of the conjugate slip system, which should occur when sufficient geometrical softening has occurred on the primary slip system due to crystal rotation, are impeded by the presence of the twins. Hence, the corresponding slip plane remains parallel to the twin plane despite multiple-slip conditions. This "overshooting" and/or "latent textural hardening" mechanism, which was first proposed by Leffers[60] strongly delays the textual transition from the Copper to the Brass orientation. At lower strains, twins act to reinforce the Copper texture generated by primary {111}⟨110⟩ slip and by suppressing multiple slipping, i.e., deformation-induced twinning promotes overshooting. As the slip is limited to planes parallel to the twinning planes, no large back-stresses can develop. Under these conditions, the strain hardening is essentially due to a pronounced planar slip caused by the presence of the initially formed twins. At higher strains, however, high stresses activate multiple-slip and secondary twin systems. The initial twins act as strong barriers to these new deformation systems and large back-stresses can develop in this stage. Hence, the strain hardening of the alloy can be dynamically increased during deformation. Therefore, a good combination of UTS and elongation to fracture is anticipated.

Figure 12 shows the texture analysis of the BCC phase (α-ferrite, and α′-martensite) for the specimens deformed up to $e = 30$ pct and $e = 70$ pct tensile strains. Figures 12(a) through (d) represent the ODF maps and related pole figures, respectively. The main components are {001}⟨110⟩, {112}⟨110⟩, and {111}⟨110⟩ which belong to the α-fiber and γ-fiber. A quantitative comparison of the ODFs is illustrated in Figure 13 by comparing the intensities along the α-fiber and γ-fiber. The intensities of the {001}⟨110⟩ and {111}⟨110⟩ components in the α-fiber and γ-fiber are increased with the

increasing in strain (Figure 13). These findings are explained by the fact that the normal deformation textures in BCC alloys consist of {111}⟨112⟩, {111}⟨123⟩, {001}⟨110⟩, {112}⟨110⟩, and {111}⟨110⟩ orientations.[61] The ferritic steels generally develop α-fiber during deformation.[42] Thus, the strong α-fiber was found in the ferrite phase of the newly designed alloy. In this case, α-fiber is developed by deformation; however, the {001}⟨110⟩, {112}⟨110⟩, {111}⟨110⟩ components (Figure 13), particularly the former, become more pronounced as the plastic strain is increased. It should be mentioned that although the deformation of the ferrite phase affects the textural development in the BCC phase, the formation of α′-martensite with a preferred orientation would have an important role in the textural evolution during straining. The findings of Łuksza et al.[62] indicated that the main texture components of SIM were related to the α-fiber = ⟨110⟩‖RD, γ-fiber = ⟨111⟩‖ND and ε-fiber = ⟨011⟩‖ND. It was explained that the main texture component of SIM in metastable single phase austenitic steels was the {001}⟨110⟩ orientation which originated from the Brass {011}⟨211⟩ orientation of the parent austenite phase following the Kurdjumov-Sachs orientation relationship.[63] Although the SIM texture has been investigated in several research studies, the results to date have been somehow inconsistent. Kumar et al. reported that the cold deformation of a 304 L metastable steel exhibited a notable sharp {001}⟨110⟩ texture component in the α′-martensite constituent.[63] They found that the main texture component of the α′-martensite phase obtained from the ODF of a 50 pct cold-deformed specimen was {001}⟨110⟩ together with a weak {112}⟨110⟩ component.[63] Other researchers have reported that the {111}⟨112⟩, {111}⟨011⟩ and {001}⟨110⟩ components of strain-induced α′-martensite appeared during the initial stage of deformation while {113}⟨110⟩, {112}⟨110⟩ and {001}⟨110⟩ orientations became predominant deformation progressed.[64] The present authors believe that prevalence of the {001}⟨110⟩ and {111}⟨110⟩ components, in particular {001}⟨110⟩ which has been observed in aforementioned literature studies, is due to the SIM transformation. All in all, it is logical to conclude that the high intensity of the {001}⟨110⟩ orientation next to the weaker {112}⟨110⟩ orientation in the present study is due to SIM transformation along with ferrite texture development during deformation.

V. CONCLUSIONS

The microstructural and deformation characteristics of a newly designed duplex ferritic–austenitic stainless steel with superior mechanical properties (900 MPa UTS and >90 pct elongation to fracture) were investigated. The findings were compared to those reported for a TRIP DSS. The main conclusions are

1. The microstructural observations showed that the austenite-deformation mechanism is of a complicated nature which includes deformation banding, strain-induced martensite formation, and deforma-

tion twinning; however, the ferrite phase was mainly deformed by a dislocation glide mechanism.

2. The stepwise deformation analysis of the newly designed DSS revealed that the improved mechanical properties, especially the enhanced total elongation could be attributed both to TRIPing over a wide strain range due to the optimized stability of austenite, and the TWIPing phenomena during straining.

3. The thermodynamic calculations on the chemical driving force of austenite-to-α'-martensite transformation ($\Delta G^{\gamma \rightarrow \alpha'}(T)$) revealed that the lower $\Delta G^{\gamma \rightarrow \alpha'}(T)$ value of the newly designed alloy with respect to the reference TRIP DSS results in a higher mechanical deriving force toward the martensitic transformation, and consequently, the TRIP effect was activated at an increased level of strain. This resulted in achieving a notably larger elongation to fracture in the newly designed DSS.

4. The texture analysis of the austenite after tensile deformation showed the presence of strengthened Copper and Rotated Brass components along with nearly constant Goss and Brass components. The main reason for Rotated Brass orientation development instead of pure Brass component was attributed to deformation mode, *i.e.*, tensile mode and SIM formation during straining which suppress the texture development along with pure Brass component. Furthermore, the intensification of the Copper component in the FCC austenite phase was ascribed to the indirect effects of deformation bands, in particular mechanical twins. Toward that end, twinning is considered to have a latent textural-hardening effect and dynamically enhances the work hardening, thereby increasing strength and plasticity of the alloy during deformation.

5. The texture analysis of BCC phase indicated the development of $\{111\}\langle011\rangle$ and $\{001\}\langle110\rangle$ orientations together with a weak $\{112\}\langle110\rangle$ component. The intensification of these components, especially $\{001\}\langle110\rangle$ orientation, was attributed to the formation of strain-induced α'-martensite during plastic straining.

REFERENCES

1. R.N. Gunn: *D1uplex Stainless Steels: Microstructure, Properties and Applications*, Woodhead Publishing, Cambridge, 1977.
2. J.Y. Choi, J.H. Ji, S.W. Hwang, and K.T. Park: *Mater. Sci. Eng.: A*, 2011, vol. 528, pp. 6012–19.
3. J.Y. Choi, J.H. Ji, S.W. Hwang, and K.T. Park: *Mater. Sci. Eng.: A*, 2011, vol. 535, pp. 32–39.
4. V. Gavriljuk and H. Berns: *High Nitrogen Steels: Structure, Properties, Manufacture, Applications*, Springer Science & Business Media, New York, 2013.
5. H. Berns, S. Riedner, and V. Gavriljuk: *High Interstitial Stainless Austenitic Steels*, Springer Science & Business Media, New York, 2012.
6. D. Raabe: *Mater. Sci. Eng.: A*, 1995, vol. 197, pp. 31–37.
7. P.D. Nezhadfar, A. Zarei-Hanzaki, S.S. Sohn, and H.R. Abedi: *Mater. Sci. Eng.: A*, 2016, vol. 665, pp. 10–16.
8. A. Mohamadizadeh, A. Zarei-Hanzaki, S. Mehtonen, D. Porter, and M. Moallemi: *Metall. Mater. Trans. A*, 2016, vol. 47A, pp. 436–49.
9. D.T. Pierce, J.A. Jiménez, J. Bentley, D. Raabe, and J.E. Wittig: *Acta Mater.*, 2015, vol. 100, pp. 178–90.
10. M. Moallemi, A. Kermanpur, A. Najafizadeh, A. Rezaee, H. Samaei Baghbadorani, and P. Dastranjy Nezhadfar: *Mater. Sci. Eng.: A*, 2016, vol. 653, pp. 147–52.
11. F. Lecroisey and A. Pineau: *Metall. Trans.*, 1972, vol. 3, pp. 391–400.
12. R.E. Schramm and R.P. Reed: *Metall. Trans. A*, 1975, vol. 6, pp. 1345–51.
13. C. Herrera, D. Ponge, and D. Raabe: *Acta Mater.*, 2011, vol. 59, pp. 4653–64.
14. J.Y. Choi, J.H. Ji, S.W. Hwang, and K.T. Park: *Mater. Sci. Eng.: A*, 2012, vol. 534, pp. 673–80.
15. J.Y. Choi, J.H. Ji, S.W. Hwang, and K.T. Park: *Metall. Mater. Trans. A*, 2012, vol. 44, pp. 597–601.
16. S. Fréchard, F. Martin, C. Clément, and J. Cousty: *Mater. Sci. Eng.: A*, 2006, vol. 418, pp. 312–19.
17. I. Toor, P.J. Hyu, and H.S. Kwon: *Corros. Sci.*, 2008, vol. 50, pp. 404–10.
18. P. Behjati, A. Kermanpur, and A. Najafizadeh: *Mater Sci Eng.: A*, 2013, vol. 588, pp. 43–48.
19. T.H. Lee, H.Y. Ha, Byoungchul Hwang, S.J. Kim, and E. Shin: *Metall. Mater. Trans.s A*, 2012, vol. 43, pp. 4455–59.
20. T.H. Lee, E. Shin, O. Chang-Seok, H.Y. Ha, and S.J. Kim: *Acta Mater.*, 2010, vol. 58, pp. 3173–86.
21. Q. Ran, Y. Xy, J. Li, J. Wan, X. Xiao, H. Yu, and L. Jiang: *Mater. Design*, 2014, vol. 56, pp. 959–65.
22. S. Curtze, V.-T. Kuokkala, A. Oikari, J. Talonen, and H. Hänninen: *Acta Mater.*, 2011, vol. 59, pp. 1068–76.
23. D.G. Brandon: *Acta Metall.*, 1966, vol. 14, pp. 1479–84.
24. G. Frommeyer, U. Brüx, and P. Neumann: *ISIJ Int.*, 2003, vol. 43, pp. 438–46.
25. M. Pozuelo, J.E. Wittig, J.A. Jiménez, and G. Frommeyer: *Metall. Mater. Trans. A*, 2009, vol. 40, pp. 1826–34.
26. G.B. Olson and M. Cohen: *Metall. Trans. A*, 1975, vol. 6, pp. 791–95.
27. G.B. Olson and M. Cohen: *J. Less Common Metals*, 1972, vol. 28, pp. 107–18.
28. Z.X. Wu, Y.W. Zhang, and D.J. Srolovitz: *Acta Mater.*, 2009, vol. 57, pp. 4508–18.
29. Y.-H. Zhao, J.F. Bingert, X.Z. Liao, B.Z. Cui, K. Han, A.V. Sergueev, and Y.T. Zhu: *Adv. Mater.*, 2006, vol. 18, pp. 2949–53.
30. F.K. Yan, N.R. Tao, F. Archie, I. Gutierrez-Urrutia, D. Raabe, and K. Lu: *Acta Mater.*, 2014, vol. 81, pp. 487–500.
31. H.T. Wang, N.R. Tao, and K. Lu: *Acta Mater.*, 2012, vol. 60, pp. 4027–40.
32. M. Sennour, S. Lartigue-Korinek, Y. Champion, and M.J. Hÿtch: *Philos. Mag.*, 2007, vol. 87, pp. 1465–86.
33. X. Guo, Q.D. Ouyang, G.J. Weng, and L.L. Zhu: *Mater. Sci. Eng.: A*, 2016, vol. 657, pp. 234–43.
34. M. Dao, L. Lu, R.J. Asaro, J.Th.M. De Hosson, and E. Ma: *Acta Mater.*, 2007, vol. 55, pp. 4041–65.
35. A. Weidner and H. Biermann: *JOM*, 2015, vol. 67, pp. 1729–47.
36. L. Remy and A. Pineau: *Mater. Sci. Eng.*, 1977, vol. 28, pp. 99–107.
37. B. Mahato, S.K. Shee, T. Sahu, S.G. Chowdhury, P. Sahu, D.A. Porter, and L.P. Karjalainen: *Acta Mater.*, 2015, vol. 86, pp. 69–79.
38. V.G. Gavriljuk, B.D. Shanina, and H. Berns: *Acta Mater.*, 2000, vol. 48, pp. 3879–93.
39. V. Gerold and H.P. Karnthaler: *Acta Metall.*, 1989, vol. 37, pp. 2177–83.
40. L. Kaufman: *Trans. Met. Soc. AIME*, 1959, vol. 215, pp. 218–27.
41. K.H. Lo, C.H. Shek, and J.K.L. Lai: *Mater. Sci. Eng.: R: Reports*, 2009, vol. 65, pp. 39–104.
42. J. Keichel, J. Foct, and G. Gottstein: *ISIJ Int.*, 2003, vol. 43, pp. 1781–87.
43. A. Rollett, F.J. Humphreys, G.S. Rohrer, and M. Hatherly: *Recrystallization and Related Annealing Phenomena*, Elsevier, Boston, 2004.

44. L. Bracke, K. Verbeken, L. Kestens, and J. Penning: *Acta Mater.*, 2009, vol. 57, pp. 1512–24.
45. S.H. Hong and D.N. Lee: *Mater. Sci. Eng.: A*, 2003, vol. 351, pp. 133–47.
46. W. Mao: *J. Mater. Eng. Perform.*, 1999, vol. 8, pp. 556–60.
47. K. Lücke: ICOTOM, Brakman et al. ed. Noordwijkerhout, 1984, p. 195.
48. P.A. Beck and H. Hu: *J. Metals (NY)* 1952, vol 4.
49. D.P. Escobar, S.S.F. de Dafé, and D.B. Santos: *J. Mater. Res. Technol.*, 2015, vol. 4, pp. 162–70.
50. N. Gey, B. Petit, and M. Humbert: *Metall. Mater. Trans. A*, 2005, vol. 36, pp. 3291–99.
51. B.C. De Cooman, J. Kim, and S. Lee: *Scripta Mater.*, 2012, vol. 66, pp. 986–91.
52. J. Keichel, J. Foct, and G. Gottstein: *ISIJ international*, 2003, vol. 43, pp. 1788–94.
53. R.E. Smallman and D. Green: *Acta Metall.*, 1964, vol. 12, pp. 145–54.
54. E. El-Danaf, S.R. Kalidindi, R.D. Doherty, and C. Necker: *Acta Mater.*, 2000, vol. 48, pp. 2665–73.
55. S. Vercammen, B. Blanpain, B.C. De Cooman, and P. Wollants: *Acta Mater.*, 2004, vol. 52, pp. 2005–12.
56. B. Ravi Kumar, B. Mahato, N.R. Bandyopadhyay, and D.K. Bhattacharya: *Mater. Sci. Eng.: A*, 2005, vol. 394, pp. 296–301.
57. D. Raabe: *Acta Mater.*, 1997, vol. 45, pp. 1137–51.
58. D. Goodchild, W.T. Roberts, and D.V. Wilson: *Acta Metall.*, 1970, vol. 18, pp. 1137–45.
59. M. Milititsky, N. De Wispelaere, R. Petrov, J.E. Ramos, A. Reguly, and H. Hänninen: *Mater. Sci. Eng.: A*, 2008, vol. 498, pp. 289–95.
60. T. Leffers: *Scripta Metall.*, 1968, vol. 2, pp. 447–52.
61. J.-J. Jonas: *Microstructure and Texture in Steels*, Springer, London, 2009, pp. 3–17.
62. J. Łuksza, M. Rumiński, W. Ratuszek, and M. Blicharski: *J. Mater.s Process. Technol.*, 2006, vol. 177, pp. 555–60.
63. B.R. Kumar, A.K. Singh, S. Das, and D.K. Bhattacharya: *Mater. Sci. Eng.: A*, 2004, vol. 364, pp. 132–39.
64. H.F.G.D. Abreu, S.S.D. Carvalho, P.D. Lima Neto, R.P.D. Santos, V.N. Freire, P.M.D.O. Silva, and S.S.M. Tavares: *Mater. Res.*, 2007, vol. 10, pp. 359–66.